



## OPEN ACCESS

# Bound-to-continuum terahertz quantum cascade laser with a single-quantum-well phonon extraction/injection stage

To cite this article: Maria I Amanti *et al* 2009 *New J. Phys.* **11** 125022

View the [article online](#) for updates and enhancements.

## You may also like

- [Getting around the cell: physical transport in the intracellular world](#)  
Saurabh S Mogre, Aidan I Brown and Elena F Koslover
- [Resonant-phonon-assisted THz quantum-cascade lasers with metal-metal waveguides](#)  
Qing Hu, Benjamin S Williams, Sushil Kumar *et al.*
- [New frontiers in quantum cascade lasers: high performance room temperature terahertz sources](#)  
Mikhail A Belkin and Federico Capasso

## Bound-to-continuum terahertz quantum cascade laser with a single-quantum-well phonon extraction/injection stage

Maria I Amanti<sup>1</sup>, Giacomo Scarlari<sup>1</sup>, Romain Terazzi<sup>1</sup>,  
Milan Fischer<sup>1</sup>, Mattias Beck<sup>1</sup>, Jérôme Faist<sup>1,3</sup>, Alok Rudra<sup>2</sup>,  
Pascal Gallo<sup>2</sup> and Eli Kapon<sup>2</sup>

<sup>1</sup> Institute of Quantum Electronics, ETH Zurich, Switzerland

<sup>2</sup> Laboratory of Physics of Nanostructures, Ecole Polytechnique Federale de Lausanne (EPFL), Switzerland

E-mail: [jerome.faist@phys.ethz.ch](mailto:jerome.faist@phys.ethz.ch)

*New Journal of Physics* **11** (2009) 125022 (19pp)

Received 24 July 2009

Published 17 December 2009

Online at <http://www.njp.org/>

doi:10.1088/1367-2630/11/12/125022

**Abstract.** A terahertz quantum cascade laser design that combines a wide gain bandwidth, large photon-driven transport and good high-temperature characteristics is presented. It relies on a diagonal transition between a bound state and doublet of states tunnel coupled to the upper state of a phonon extraction stage. The high optical efficiency of this design enables the observation of photon-driven transport over a wide current density range. The relative tolerance of the design to small variations in the barrier thicknesses made it suitable for testing different growth techniques and materials. In particular, we compared the performances of devices grown using molecular-beam epitaxy with those achieved using organometallic chemical vapor deposition. The low-threshold current density and the high slope efficiency makes this device an attractive active region for the development of single-mode quantum cascade lasers based on third-order-distributed feedback structures. Single-mode, high power was achieved with good continuous and pulsed wave operation.

<sup>3</sup> Author to whom any correspondence should be addressed.

**Contents**

<b>1. Introduction</b>	<b>2</b>
<b>2. Design and simulations</b>	<b>3</b>
2.1. Population inversion: architectures . . . . .	3
2.2. Energy states and dipoles . . . . .	6
2.3. Lifetimes . . . . .	6
<b>3. Growth and processing</b>	<b>9</b>
<b>4. Light–current and voltage–current characteristics</b>	<b>10</b>
4.1. Doping and growth dependence of the performances . . . . .	10
4.2. Discussion of the transport characteristics . . . . .	13
4.3. Temperature dependence of the performances . . . . .	14
<b>5. Magnetotransport</b>	<b>15</b>
<b>6. Distributed feedback QCL</b>	<b>16</b>
<b>7. Conclusion</b>	<b>17</b>
<b>Acknowledgments</b>	<b>18</b>
<b>References</b>	<b>18</b>

**1. Introduction**

The terahertz frequency range, loosely defined as the spectrum between 1–10 THz, has traditionally been lacking convenient optical sources. Terahertz radiation has some important potential applications [1, 2] in imaging, chemical sensing and telecommunications. The long wavelength of terahertz radiation enables good penetration into heavily diffusing materials such as foams or small-grained material. The vibrational modes of large organic and inorganic molecules are in the terahertz region, offering potential avenues for label-free sensing of DNA [3]. The terahertz range has also some very interesting radio-astronomical applications, as it houses, among other important spectral signatures, the brightest cooling lines of the dense interstellar medium ([CII] 158  $\mu\text{m}$ , [OI] 63 and 145  $\mu\text{m}$ ) present in space. Because of the lack of transparency of the atmosphere in the terahertz region, such observation must be performed from airborne or spaceborne telescopes such as SOPHIA [4], putting additional constraints on the optical sources.

For this reason, there is a strong interest in the development of terahertz sources that are tunable, portable and manufacturable in quantities. Recently, much progress has been made in sources based on nonlinear generation from either ultrafast lasers or continuous wave near-infrared or even mid-infrared [5] sources. Compared with these techniques based on nonlinear mixing, fundamental oscillators have the potential advantage of offering higher efficiencies and an easier fabrication technology.

The operation of quantum cascade lasers [6] was first achieved in the terahertz in 2001 at a frequency of 4.1 THz, in pulsed mode and up to a maximum operating temperature of 65 K [7]. Continuous wave operation was achieved shortly thereafter [8], followed by operation above liquid nitrogen temperatures [9]. The introduction of a design based on resonant optical phonon extraction [10] combined with the use of metal–metal waveguides [11] has enabled a significant increase in the maximum operating temperature achieved by these devices, up to

a maximum temperature of 186 K [12]. Even if this last result is a significant improvement compared with the first generation devices, it still lies significantly below the temperatures achievable by thermoelectric cooler based on Peltier effects.

Another challenge was to explore to what extent the operating range of these devices could be expanded beyond the first range of operation of 3–4 THz. On the low-frequency side, optimization of the design of a bound-to-continuum transition lead to operation at 2.3 THz [13] and subsequently at 1.9 THz [14]. The addition of an electron reservoir energetically decoupled from the miniband-enabled operation of these devices down to a frequency of 1.2 THz [15, 16].

So far, applications of terahertz quantum cascade lasers have been restricted to proof-of-principle applications, even though some very encouraging results have already been achieved [17]. Real-time, stand-off imaging using a microbolometer camera has also been demonstrated [18]. Imaging of biological material with potential relevance for therapy was recently reported [19]. The results closest to a final application have been demonstrated in radio-astronomy: quantum cascade lasers have been used as local oscillators, pumping a hot electron bolometer and demonstrating a competitive receiver noise temperature [20]. Another important step is the report, recently achieved [21], of phase-locking of a THz quantum cascade laser onto a microwave reference.

For many of these applications, the challenge is to find a quantum design that offers at the same time a good manufacturability, high wallplug efficiency, and a high maximum operating temperature. Usually, a broad gain bandwidth is an advantage as it allows devices at various wavelengths to be fabricated from the same epilayer material.

In this paper, we want to evaluate a design based on a short bound-to-continuum transition with a one-well injector operating around 3 THz. The design is described and studied theoretically in section 2. In section 3, a brief description of the growth and processing of the devices grown either by molecular beam epitaxy (MBE) or by organometallic chemical vapor deposition (OMCVD) is presented. In section 4, we report the characterization of such devices in operating temperature and slope efficiency. The results of magnetospectroscopy are reported in section 5. In section 6, we report the results of third-order-distributed feedback quantum cascade lasers fabricated using this laser material.

## 2. Design and simulations

### 2.1. Population inversion: architectures

Gain between subbands depends critically on the population inversion. As noted very early in the context of mid-infrared quantum cascade lasers [22, 23] and using the notations shown schematically in figure 1, the population inversion is maximized by achieving the largest ratio of upper to lower lifetime  $\tau_{32}/\tau_2$ , a large injection efficiency in the upper state  $\eta$ , and a long upper state lifetime  $\tau_3$ . The standard approach used in mid-infrared quantum cascade lasers has been to use the properties of the intersubband non-radiative transitions to achieve a large ratio of lifetimes, and to employ a resonant tunneling injection of the electrons from the injector into the upper state to obtain a high value of  $\eta$ . For terahertz quantum cascade lasers, a similar approach has worked very well at cryogenic temperatures. The active region architecture of the first quantum cascade laser operating in the terahertz [7] is essentially a scaled version of a mid-infrared chirped-superlattice active region [24], in which the population inversion

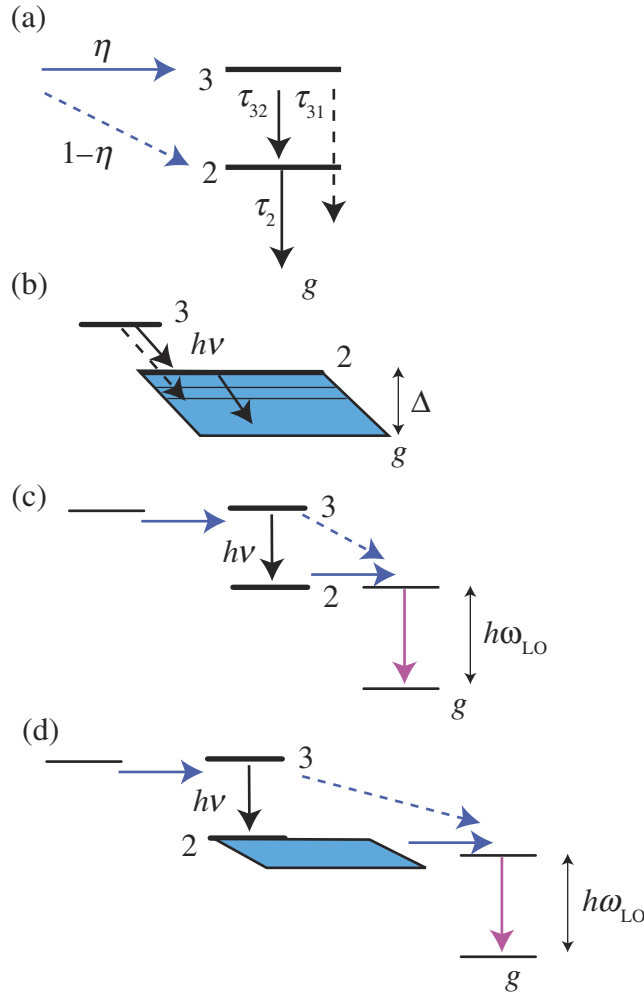


**Figure 1.** (a) Schematic levels of a generic quantum cascade laser. By tradition, the upper level is labeled 3. (b) Bound-to-continuum or superlattice design. (c) Design based on a resonant tunneling extraction on an optical phonon resonant stage, as demonstrated by the MIT group [10]. (d) Bound-to-continuum with optical phonon resonant extraction stage.

between the two states at the edge of the miniband is obtained by a phase space argument. The scattering rate from the lower state  $\tau_2^{-1}$  is very large, the latter being the upper state of the lower miniband while the scattering from the upper state is similarly spread among the whole lower miniband, keeping the scattering rate into the lower state small, i.e.  $\tau_{32}^{-1} \ll \tau_2^{-1}$ . Similarly, the bound-to-continuum approach reported in [9] is a transposed version of the same approach demonstrated at shorter wavelengths [23, 25]. In the bound-to-continuum design, the population inversion achieved by a combination of the phase space used in the superlattice active region with a diagonal transition between states with a reduced spatial overlap, further enhancing the population inversion. The bound-to-continuum approach was further developed [13, 26] and yielded devices with a very high slope efficiency and power at temperatures of about 20 K. However, the maximum operating temperature of these devices remained limited to about 100 K. The problem originates from the scaling of the miniband width  $\Delta$  with photon

energy  $h\nu$ , considering the effect of temperature  $kT$  and the broadening of the individual levels  $\Gamma$ . For the miniband and bound-to-continuum approach to succeed, one should maintain the miniband width much larger than the broadening of the individual levels  $\Delta \gg \Gamma$  and larger than the thermal energy  $\Delta > kT$ . In the mid-infrared, at room temperature ( $kT = 26$  meV) the conditions are satisfied because  $\Delta = 100\text{--}150$  meV  $\gg \Gamma \approx 5\text{--}10$  meV and  $\Delta > kT$ . In the terahertz, however, the same inequality only holds at cryogenic temperature because the miniband width is only 15 meV, while the broadening at room temperature remains of the order of a few meV. Similarly, one cannot keep a very wide miniband  $\Delta = 100$  meV with a photon energy of  $h\nu = 15$  meV, as the latter should be much larger than the individual level spacing of the miniband. In addition, as soon as the sum of the miniband width and the photon energy becomes equal or larger than the optical phonon energy  $\Delta + h\nu > \hbar\omega_{\text{LO}} = 36$  meV, the lifetime of the upper state drops very strongly even at low temperatures. As a result, no terahertz laser has ever been demonstrated to operate in this regime. In fact, there are no combinations of states where population inversion has been demonstrated for temperatures significantly larger than 100 K solely based on intersubband scattering.

As shown schematically in figure 1(c), coupling by resonant tunneling the lower state of the laser transition to a very short-lived upper state of a nearby well allows a significant reduction of the lower state lifetime while preserving a long upper state lifetime. This idea is the basis of the so-called resonant phonon design first demonstrated by the MIT group [10]. This design has seen many variations [27, 28] and the current version has demonstrated the highest operating temperature of a THz quantum cascade laser so far [12]. The low lifetime of the upper level of the well following the active region is usually achieved by spacing the levels resonantly with an optical phonon energy. In this way, the condition  $\Delta > kT$  is satisfied. This architecture has the additional benefit of shifting the intersubband absorption of the electrons from the ground state of the quantum well to a photon energy larger than the laser transition. The transfer of some or all of the oscillator strengths from the ground state from very low frequencies to frequencies above the transition energy was one of the key ingredient for the achievement of intersubband lasers between 1.2–2 THz [16]. In that case, the pair of states were spaced by less than the optical phonon energy. A general feature of these designs is the requirement for a simultaneous alignment of the injector and extraction stage at the same electric field [29]. Such a double resonance condition, however, increases the sensitivity of the design to growth inaccuracies.

A third class of designs aims at combining the advantages of both approaches. As shown schematically in figure 1(d), the active stage is based on a bound-to-continuum transition, while the miniband is coupled to an extractor quantum well [30]. This architecture has the advantage of reducing the direct coupling between the upper state and the extractor well since they are physically separated by the length of the miniband region. The alignment condition on the extraction stage is also somewhat relaxed by the fact that it has to be satisfied over the width of the miniband and no longer over the one of a single state. The original design following this architecture [30] was based on a five-quantum-well active region and two-quantum-well injector region. In this paper, we report on the study of a shortened version of this design, where the total number of quantum wells has been reduced to four, with a three-quantum-well active region coupled to a one-quantum-well injector. The latter choice was made to increase the maximum operating temperature of the device. A four-quantum-well structure with a single well injector was also reported in [31]; that structure had, however, a very different active region with a much larger oscillator strength.

In a quantum cascade laser, in the limit of vanishing waveguide losses, the gain must only balance the losses of the active region itself. As a result, in a simplified model, it can be shown [32] that a figure of merit for the active region can be expressed as a product of a normalized gain cross section  $g^*$  and a normalized lifetime  $\tau^*$ , with

$$g^* = f' \omega^2 \tau_{\parallel}^2, \quad (1)$$

where  $f'$  is the normalized oscillator strength of the laser transition at angular frequency  $\omega$  and  $\tau_{\parallel}$  the lifetime associated with the intersubband broadening. The normalized lifetime  $\tau^*$  is given by

$$\tau^* = \frac{\tau_{\text{up}}}{\tau_{\text{trans}}}, \quad (2)$$

where  $\tau_{\text{up}}$  is the effective upper state lifetime and  $\tau_{\text{trans}}$  the transit time across the whole active region. In a simple model of transport, the transit time increases with the number of states of the active region that are thermally populated. The latest results in high-temperature operation of terahertz quantum cascade lasers agree with this consideration, as the highest operating temperatures are achieved with designs based on three quantum wells [5, 12] and a total of four levels including the upper state one. An additional benefit of these designs with a reduced number of quantum wells is the fact that the transport can be driven by the photon field, as all other states apart from the upper one contribute very weakly to the transport time. Compared with designs with more quantum wells, these devices suffer however from inherently large leakage currents.

## 2.2. Energy states and dipoles

A schematic band diagram of the structure is shown in figure 2. Shown also are the energies and electron probability densities, computed in the extended basis spanning the whole period length. The key parameters of the design, computed using a self-consistent Schrödinger–Poisson solver, are listed in table 1. The latter can either use population obtained assuming a uniform thermal distribution or the transport populations obtained from the solution of the density matrix problem. However, because of the low doping, the correction to the potential remains small regardless of the assumption on the electron distribution. The two distributions are compared in figure 3 at a temperature of 150 K. For this reason, in the simulations we assumed, for simplicity, a uniform electronic temperature 50 K above the lattice one. The oscillator strength is concentrated mainly on the transition between levels five and four of the active region. As shown in figure 2, the wavefunctions of these two states have a relatively weak spatial overlap, that translates into a reduced normalized oscillator strength  $f' = m^* f = 0.31$ . As expected for such a diagonal transition, the scattering rate from optical phonons yields still a relatively long lifetime at elevated temperature ( $\tau = 1.9$  ps at 150 K).

## 2.3. Lifetimes

As shown in figure 2, the wavefunction of the lower state  $n = 4$  spans the complete length of the active region of the structure. As a result, it is expected that the computed value of the lower state lifetime depends on the assumption on the coherence length of the electron. In this situation, a description in a local basis [29], where the period is split between an active region (first three quantum wells) and the extractor well, is physically a more meaningful approach.



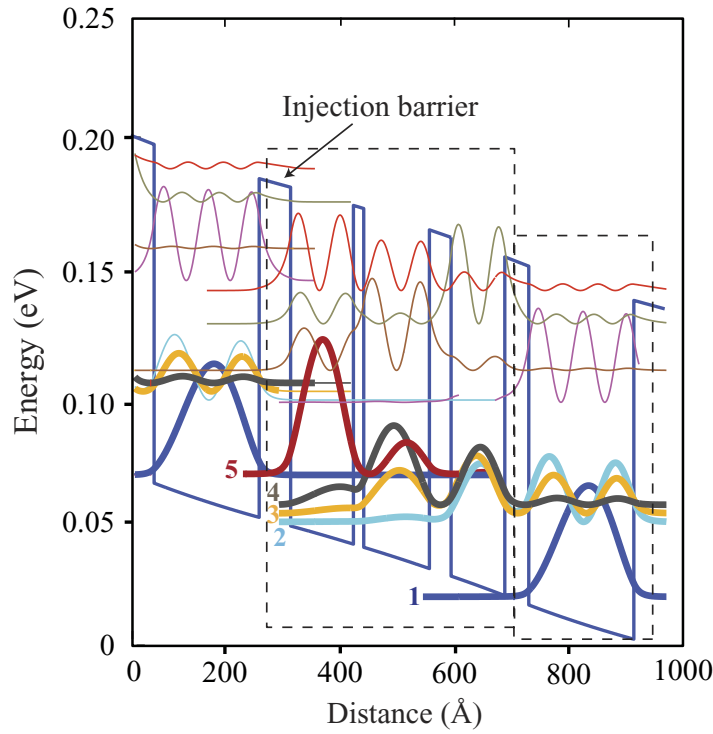


**Figure 2.** Schematic conduction band diagram of one stage of the structure EV1116 under an applied electric field of  $7.6 \times 10^3 \text{ V cm}^{-2}$ . The moduli squared of the relevant wavefunctions are shown. The layer sequence of one period of structure, in nanometers, right to left and starting from the injection barrier is **5.5**/11.0/**1.8**/11.5/**3.8**/9.4/**4.2**/18.4 where  $\text{Al}_{0.15}\text{Ga}_{0.85}\text{As}$  layers are in bold, GaAs in roman and underlined number correspond to doped layer with Si to  $N_d = 2 \times 10^{16} \text{ cm}^{-3}$ . The dashed boxes represent the position of the local basis.

**Table 1.** Key computed parameters of the structure.  $\hbar\omega$  is the photon energy,  $z$  the dipole matrix element,  $f$  the oscillator strength,  $f' = f * m^*$  the normalized oscillator strength,  $\Omega_i$  the coupling energy between the upper state and the injector level of the previous period,  $\Omega_e$  the coupling energy between the lower states and the upper state of the extractor well,  $F_{\text{NDR}}$  the field at the anticrossing and  $\tau_{150}$  the upper state lifetime at 150 K.

$\hbar\omega$	$z$	$f$	$f'$	$\Omega_i$	$\Omega_e$	$F_{\text{NDR}}$	$\tau_{150}$
12 meV	44 Å	5.5	0.36	0.5 meV	1 meV	7.6 kV cm <sup>-1</sup>	1.9 ps

In fact, we focus on the lifetime values at elevated temperature, where the in-plane dephasing rate  $\tau_{\parallel}^{-1}$  is close to the coupling energy  $\hbar\Omega_e$  between the lower state and the upper state of the extractor quantum well. To measure the in-plane dephasing rate, the transmission of the active region at terahertz frequency was measured using an ultrafast laser source and the results fitted using a Drude model [33]. Assuming this value, we compute a product  $\Omega_e\tau_{\parallel} = 0.76$  at 150 K. In the local basis, the lower state lifetime can be written as (neglecting the second-order scattering



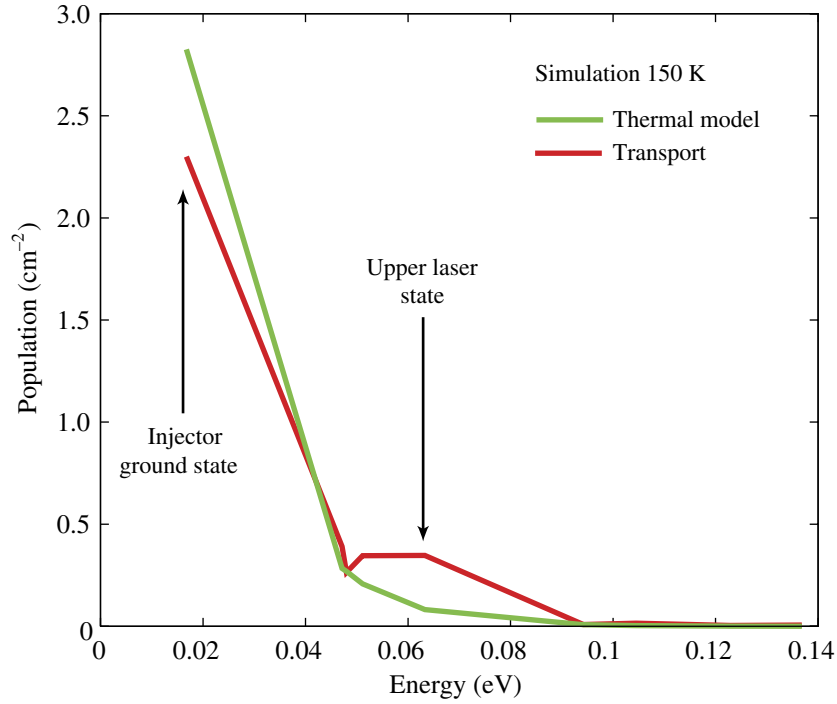


**Figure 3.** The subband populations versus the energy accounted from the bottom of the conduction band (red). The transport populations computed from the density matrix problem (green). The electrons distributed thermally for a temperature of 150 K. As shown by the red curve the population inversion is almost zero for this temperature.

terms [34] for simplicity):

$$\tau_l = \frac{1 + \Delta_e^2 \tau_{\parallel}^2}{2\Omega_e^2 \tau_{\parallel}} + 2\tau_e, \quad (3)$$

where  $\Omega_e$  is the coupling energy and  $\Delta_e$  the detuning between the lower state and the upper state of the extractor well with lifetime  $\tau_e$ . The above relation well expresses the limitation of the scheme based on resonant tunneling extraction: even in the limit of very strong coupling ( $\Omega_e \tau_{\parallel} \gg 1$ ) the lower state lifetime  $\tau_l$  cannot decrease below  $2\tau_e \approx 1$  ps. As a reference, the lifetime of the upper state of a square quantum well decreases from a value of 1.1 to 0.6 ps between 200 and 300 K. These values stress the challenge of designing a THz quantum cascade laser based on resonant tunneling extraction that would operate above 200 K. The computed value of the lifetimes for our structure and using the above approach is shown in figure 4(a). The computation includes optical phonon, intersubband roughness and impurity scatterings [35]. As expected, the upper and lower states lifetime cross at a temperature slightly above 230 K, defining a clear absolute maximum in the operation temperature to achieve population inversion.

Transport and gain have been computed using a theory based on density matrix theory [34]. Electron temperature was assumed to be uniform in the whole device, and for simplicity assumed to be larger than the lattice one by 50 K; electron–electron scattering was, however, not explicitly introduced. The computed current–voltage characteristics, computed at a lattice temperature of 100 and 150 K, are reported in figure 4(b). The gain was also computed as

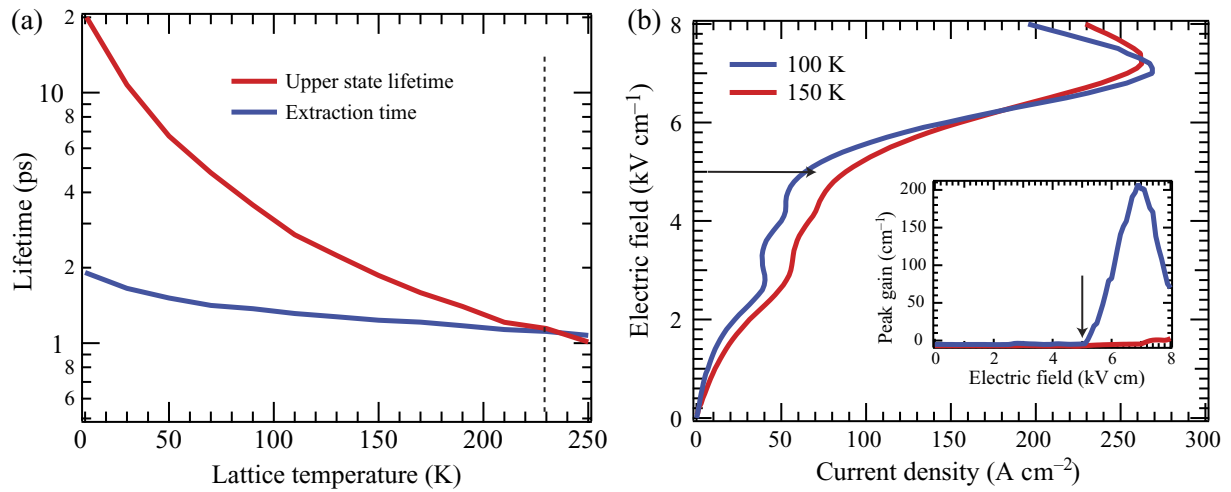


**Figure 4.** (a) Computed value of the upper  $\tau_u$  and lower state lifetimes  $\tau_l$  as a function of temperature. (b) Voltage–current characteristics, computed for a temperature of 100 and 150 K. Inset: computed gain as a function of injected current at the same temperatures.

**Table 2.** Structural characteristics of the samples studied in this work.  $d_{inj}$  and  $d_{extr}$  refer to the injection and extraction barrier thickness, respectively,  $n_s$  is the sheet density per period and  $\frac{\Delta L_{per}}{L_{per}}$  the deviation from the nominal thickness of the grown layers.

Sample	Growth	$d_{inj}$ (Å)	$d_{extr}$ (Å)	$N_{per}$	$n_s$ (cm <sup>-2</sup> )	$\frac{\Delta L_{per}}{L_{per}}$ (%)
N907	MBE	55	48	160	$1.1 \times 10^{11}$	+0.6
EV1116	MBE	55	48	180	$5.5 \times 10^{10}$	-2.7
EV1157	MBE	55	48	180	$3.7 \times 10^{10}$	-2.4
3025A	OMCVD	48	39	158	$7 \times 10^{10}$	+5
3057A/B	OMCVD	48	39	158	$1.8 \times 10^{11}$	0

a function of electric field strength for these two temperatures and plotted in the inset. As shown in the following section, the general features of the 4, as well as the maximum operating temperature, are well reproduced experimentally.

### 3. Growth and processing

The samples were grown using either solid-source MBE or OMCVD on GaAs substrates using standard growth conditions described in more details in [36, 37]. The samples studied as well as their main characteristics are listed in table 2. It was found that the properties of the OMCVD grown samples were dependent on the misorientation of the substrate. The two OMCVD samples (3057A,B) were grown in the same run on substrates with the same misorientation (2°), but oriented towards different crystallographic directions (111) A or (111) B. Only the sample 3025A, misoriented towards (111) A was measured.

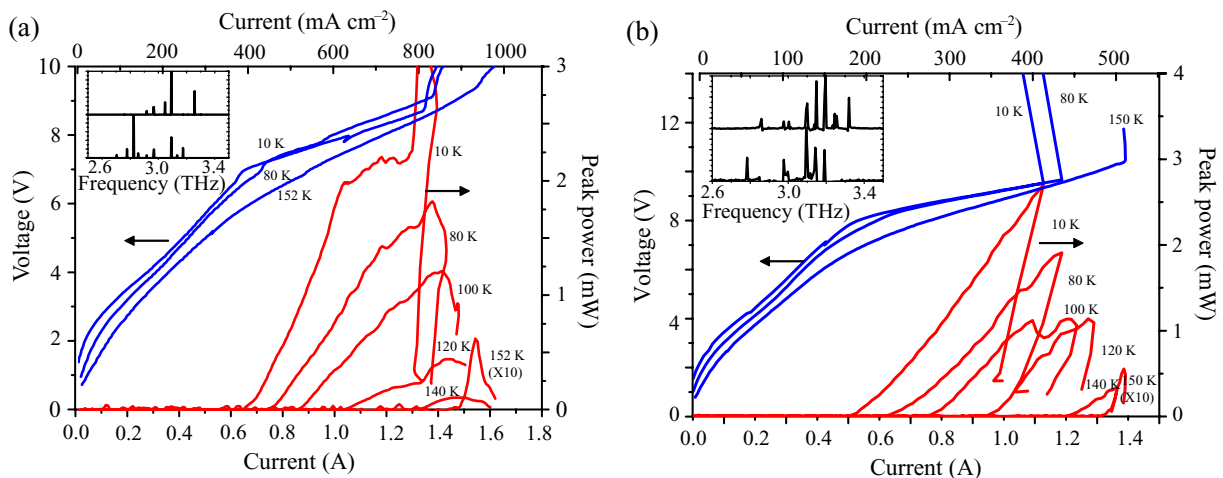


**Figure 5.** Light and bias-voltage versus current characteristics in pulsed mode of two samples for various representative temperatures. The samples are 1 mm long and 150  $\mu\text{m}$  wide. (a) N907, with a higher doping. (b) EV1116, with a lower doping. Insets: representative spectra of the devices operated in pulsed mode.

As much as possible, the samples were processed using similar steps. After a first Ti/Au metalization, the sample is wafer bonded on a GaAs carrier substrate. The sample substrate is then removed by selective etching, the etch stop layer removed and ridges are processed by wet or dry etching. After processing, the samples were cleaved, indium soldered and wire-bonded on copper submounts.

#### 4. Light–current and voltage–current characteristics

The samples were mounted on the cold head of a He flow-cryostat. The light- and bias-versus current characteristics were measured in pulsed mode as a function of the temperature. All the optical power measurements were carried out either in pulsed or continuous wave with a terahertz absolute power meter (Thomas Keating Ltd) without any intermediate optics due to the large surface of the detector.

##### 4.1. Doping and growth dependence of the performances

The light versus current characteristics of the MBE-grown sample N907, relatively heavily doped, is reported as a function of temperature in figure 5(a). The maximum operation temperature achieved in the device shown is 152 K. A lower doped version of the same layer, EV1116, shows very similar characteristics and reached a maximum operating temperature of 150 K for the device shown in figure 5(b) and of 160 K for the best device. Both samples exhibited a fairly wide emission spectrum spanning between 2.8 and 3.2 THz. The characterization of the samples reported in table 2 was performed in a similar way. The key results are reported in the table 3. The voltage–current and light-current of the two samples grown by OMCVD are reported in figure 6, along with an atomic force microscopy image of a representative surface. As shown by the comparison of the two images, both the amplitude of the roughness as well as its characteristic periodicity are very different. A statistical analysis of

**Table 3.** Key experimental results for samples studied.

Sample	$\nu$ (THz)	$J_{\text{th}}$ (10 K)	$J_{\text{NDR}}$ (10 K)	$T_{\text{max}}$ (K)	$J_{\text{max}} (T_{\text{max}})$
N907	3.1	390 A cm <sup>-2</sup>	810 A cm <sup>-2</sup>	152	920 A cm <sup>-2</sup>
EV1116	3.1	200 A cm <sup>-2</sup>	400 A cm <sup>-2</sup>	160	520 A cm <sup>-2</sup>
EV1157	3.1	175 A cm <sup>-2</sup>	225 A cm <sup>-2</sup>	140	430 A cm <sup>-2</sup>
3025A	2.65	360 A cm <sup>-2</sup>	580 A cm <sup>-2</sup>	140	700 A cm <sup>-2</sup>
3057A	3.0	600 A cm <sup>-2</sup>	900 A cm <sup>-2</sup>	150	1050 A cm <sup>-2</sup>
3057B	3.1	820 A cm <sup>-2</sup>	1420 A cm <sup>-2</sup>	150	1640 A cm <sup>-2</sup>

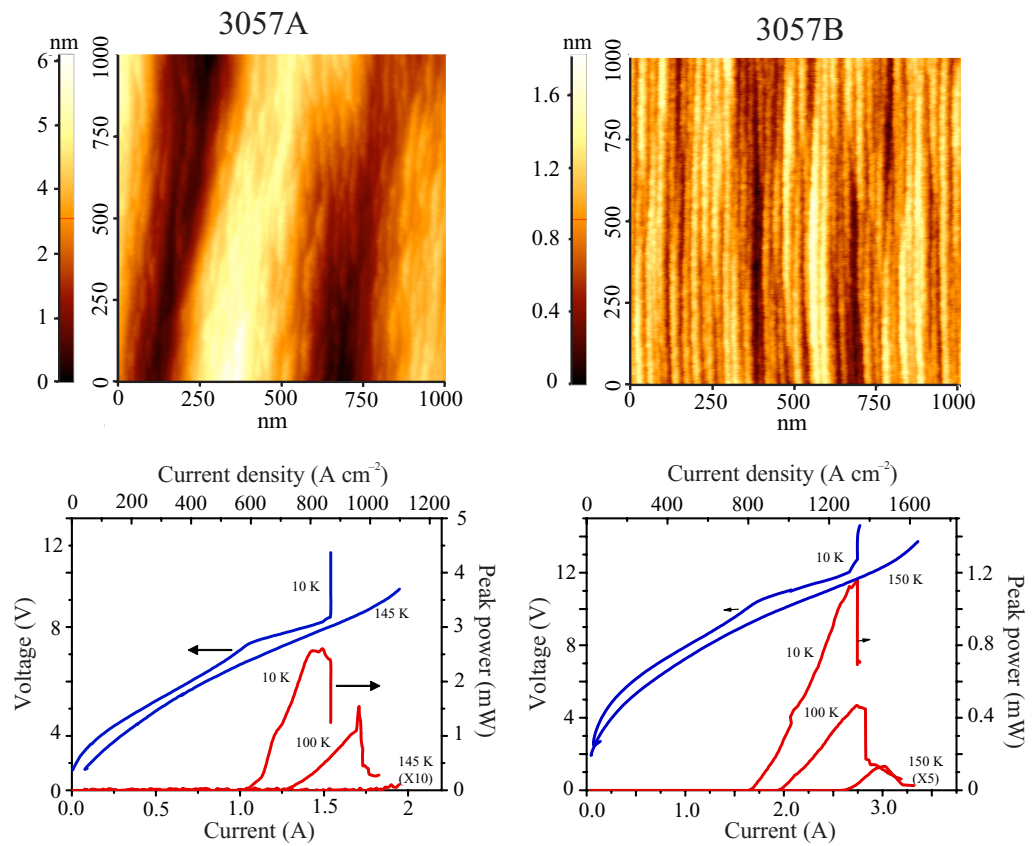


**Figure 6.** Comparison of two devices grown in a single OMCVD run using two substrates with different misorientations, 2° either towards the (111)A (3057A, left panel) or the (111)B direction (3057B, right panel). As shown by the atomic force microscopy images (top), the surfaces have a different microscopic roughness. The sample misoriented towards the (111)B direction shows a wider dynamical range and a higher maximum operating temperature. We attribute the higher maximum and threshold current of the latter device to a higher incorporation of silicon impurities during growth.

the two atomic force microscopy (AFM) images shows a root-mean-square amplitude of the roughness of 1 nm, with a characteristic length of 500 nm for the sample misoriented towards (111)A whereas the amplitude drops to 280 pm over about 50 nm for the misorientation towards

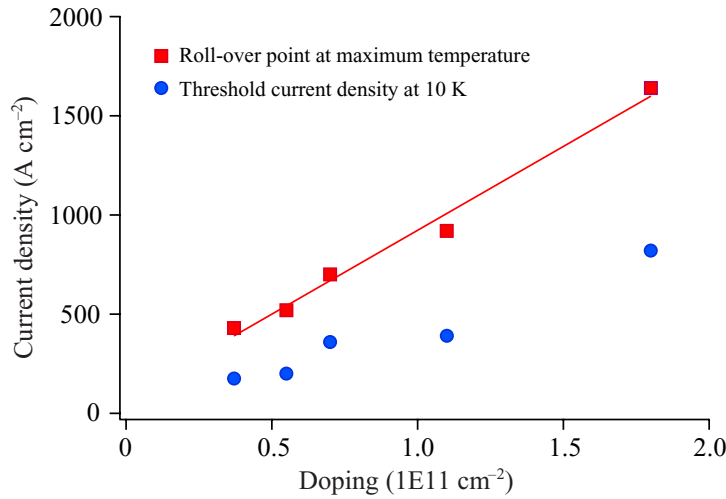


**Figure 7.** Maximum current at the optical roll-over point at the maximum temperature (squares) and threshold current density at 10 K (filled disks) versus sheet carrier density of the active region  $n_s$  for the samples specified in table 2. Sample 3057A was, however, omitted as it displayed lower performances than 3057B. The slope of the curve yields the minimum transport time across a period  $\tau_{\text{trans}} = 19$  ps. The fact that the threshold current density extrapolates to zero for vanishing doping is a strong indication that the threshold current density is limited by the voltage-current characteristics rather than by the active region losses.

(111)B. The higher operating temperature, as well as the wider dynamical range shown by the sample with the misorientation directed towards (111)B is consistent with the smaller amplitude of the interface roughness, and the results originating from this sample are reported in the table 3. We attribute the higher maximum current reached by the sample misoriented towards (111)B to a stronger incorporation of the silicon impurities. The maximum current at the onset of negative differential resistance at the maximum temperature (i.e. at 150 K), as well as the threshold current at 10 K are reported in figure 7. According to these data, we note that both the roll-over point at the maximum operating temperature and threshold currents are, in a good approximation, proportional to the active region doping. Such a result was already obtained for the case of bound-to-continuum active region designs [38]. They indicate that the electron–electron interactions remain weak up to the maximum doping of the samples studied. In addition, the performance of the devices with thinner injection and extraction barriers, are similar to the reference ones, showing that the transport is not limited by the tunneling rate in and out of the active region. The slope of the  $J_{\text{max}}$  versus  $n_s$  yields the average transport time across one period. The value found for this design is  $\tau_{\text{trans}} = 19$  ps. As a result, in our structure the value of the effective time  $\tau^*$  drops to 0.1 at 150 K. As the upper state lifetime is fixed by optical phonon scattering, the challenge would be to find ways of further decreasing the transport time to improve  $\tau^*$ . As expected, the diagonal three-quantum-well structure reported recently [12] exhibits a shorter value of the transit time, but at the cost of a larger leakage current for the same doping. The fact that the threshold current density is found to be linear as a function of doping had been interpreted in two ways. In [38], it was argued that, in a similar

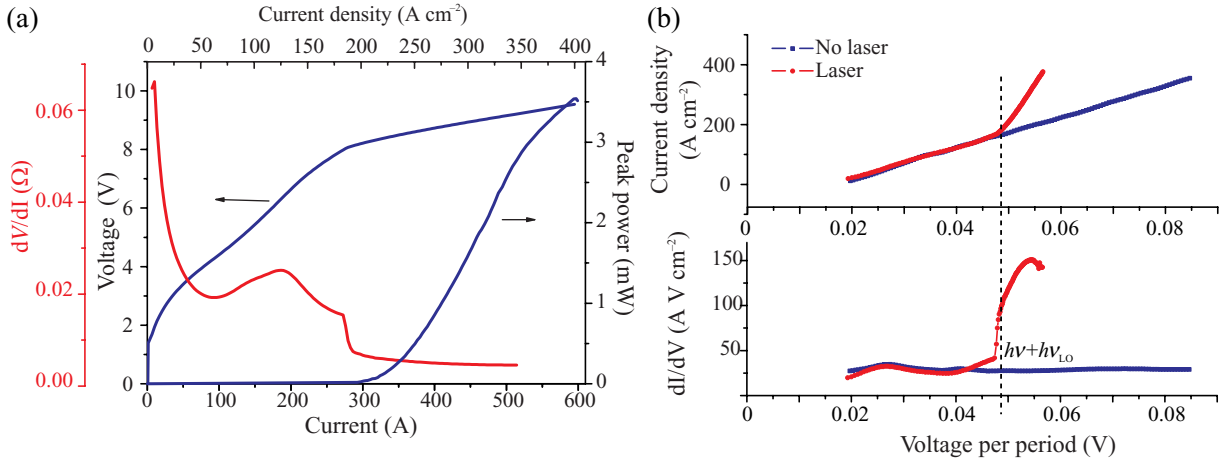


**Figure 8.** (a) Light, current and differential resistance characteristics versus applied bias for the sample EV1116 measured in continuous wave. (b) Current density (top panel) and differential conductance (bottom panel) as a function of the applied bias per period for a lasing and a non-lasing device.

way as what is occurring in mid-infrared quantum cascade lasers, the active region optical losses are dominated by the tails of intersubband absorption from the electrons of the injector. As a result, the threshold current is expected to increase linearly with active region doping. However, in other studies of active regions based on resonant phonon extraction [39, 40], it was argued that the laser threshold is controlled by the voltage and not by the current through the active region losses, and therefore the threshold current dependence in doping is a simple result of the scaling of the current–voltage characteristics. The waveguide losses have two different origins: on the one hand, there are the active region optical losses, that are expected to grow linearly with doping; on the other hand, the losses originating from the metal contacts are of course independent from doping. As a result, we expect the threshold current density to extrapolate to a nonzero value, representing the contribution of the metal losses to the threshold, for vanishing doping; whereas a zero value is expected for a threshold current controlled by voltage. Inspection of these characteristics for our devices shows that, in contrast to the bound-to-continuum samples discussed in [38], we are in a situation where the threshold current is mostly controlled by the applied bias. As discussed later, we understand that this voltage-controlled behavior is a feature of designs with low number of active wells and more specifically of devices with single-quantum-well injectors.

#### 4.2. Discussion of the transport characteristics

The voltage, light and differential resistance versus current characteristics of device EV1116 are shown in figure 8(a) in continuous wave operation. The maximum of differential resistance appearing at  $120\ A\ cm^{-2}$  corresponds to the situation where the injector is aligned between the lower and the upper states. After a decrease of the differential resistance accompanying the alignment of the injector with the upper state of the laser transition, laser threshold is reached at a current density of  $175\ A\ cm^{-2}$ , accompanied by a very sharp change of slope of the current–voltage characteristics. The current in the laser device reaches  $400\ A\ cm^{-2}$  before

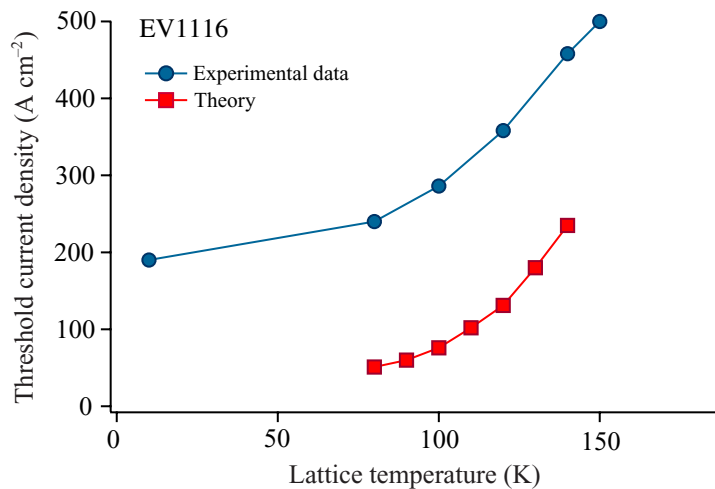


**Figure 9.** Comparison of the computed and experimental threshold current density as a function of temperature for sample EV1116.

the device enters the negative differential resistance region (NDR). To get a further insight into the device characteristics, the experimental data are replotted as a function of bias period, and compared in figure 8(b) to the one of a non-lasing device, obtained by processing a layer into a very high optical loss cavity. Although both devices were measured at a holder temperature of 10 K, the lattice temperature is significantly higher due to self-heating. This effect is especially strong in the case of the non-lasing device because of its relatively large size ( $200\ \mu\text{m} \times 1\ \text{mm}$ ). The non-laser device shows a relatively smooth voltage–current characteristics. As expected, the laser device turns on at a bias corresponding to the sum of the photon and longitudinal phonon energies. The onset of photon-driven transport corresponds to a strong increase in the current and differential conductance. By subtracting the current density at the onset of NDR for the laser and non-laser samples, we obtain a radiative current density of  $164\ \text{A cm}^{-2}$ , marginally smaller than the non-radiative one. As a result, we can infer a total internal quantum efficiency of 41% for this device. The external efficiency is much lower because only a small fraction of the total optical power is extracted from the device and collected by the optical power measurement. The differential efficiency can be extracted from the ratio of the differential conductances below and above threshold and is found to be as high as 80%.

#### 4.3. Temperature dependence of the performances

The threshold current density for device EV1116 is plotted as a function of the temperature in figure 9 and compared to the results of the density matrix model. The theoretical value of the maximum operating temperature (140 K) is close but lower than the experimental one (160 K). However, the experimental thresholds are larger than the predicted ones. This is not very surprising as the theoretical model does not include electron–electron scattering, whose influence cannot probably be neglected at low temperature. Accordingly, assuming the usual temperature dependence of the threshold current with temperature  $J = J_0 \exp(T/T_0)$ , the theoretical model predicts a value of the  $T_0 = 37\ \text{K}$  lower than the one  $T_0 = 90\ \text{K}$  experimentally observed.



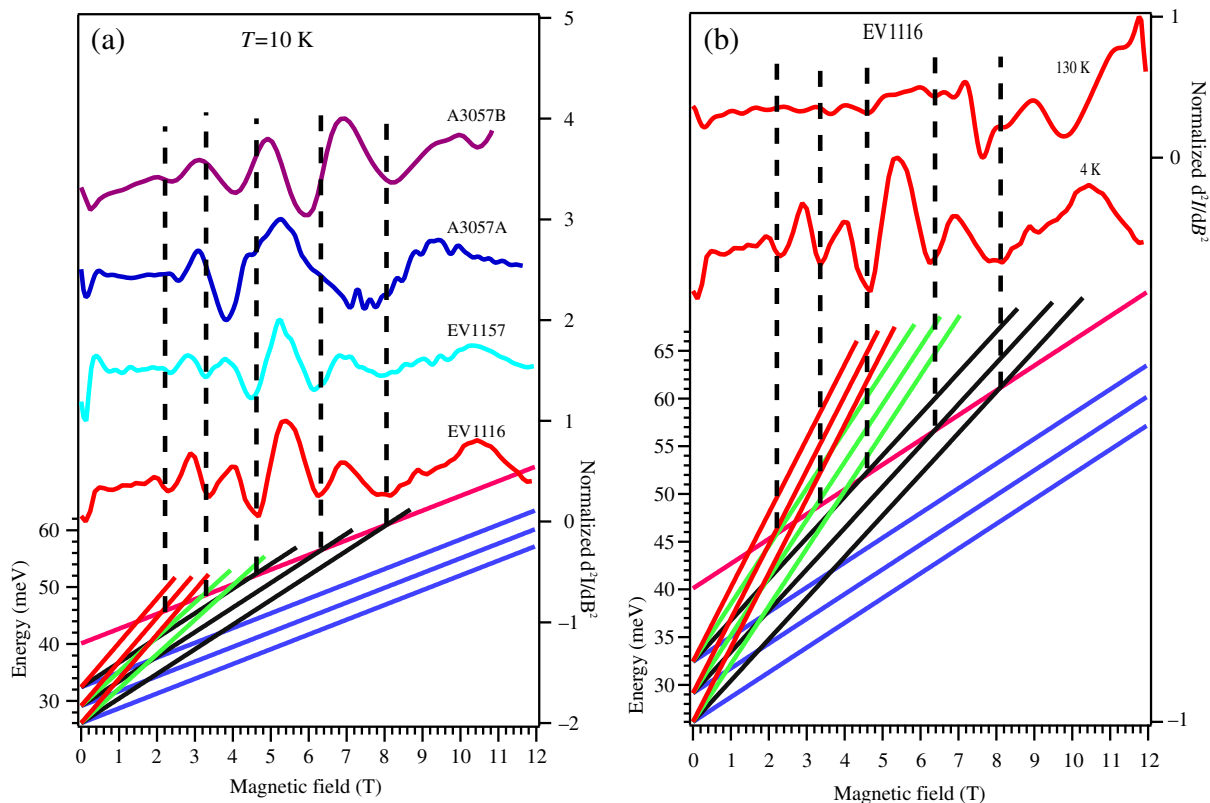


**Figure 10.** (a) Comparison of the magnetotransport data on various samples. The applied electric field is  $6.5 \text{ kV cm}^{-1}$ , lower than the threshold one to minimize overheating. Top panel, second derivative of the current–magnetic field data as a function of magnetic field. Lower panel, the fan diagram of the Landau levels as a function of magnetic field. Crossing between the upper state Landau level and one of the lower state Landau level should correspond to a maximum of the second derivative characteristics. (b) Comparison of the magnetotransport characteristics at low temperature (10 K) and close to the maximum operating temperature (130 K). The applied field is  $6.5 \text{ kV cm}^{-1}$ .

## 5. Magnetotransport

As shown by the performances reported in figure 6 and as found previously [37], we find that the samples grown by MBE and OMCVD exhibit, for comparable dopings, similar threshold current densities and maximum operating temperatures.

It was shown [41, 42] that the study of the electron transport in a strong perpendicular magnetic field is a sensitive probe of the position and broadening of the active region states. The successive crossing of the Landau-level ladder associated with each of the lower states of the active region gives rise to a maximum of the current for the bias and magnetic field corresponding to this Landau-intersubband resonance. For this reason, the second derivative of the current–magnetic field characteristic is shown in figure 10(a) for four representative samples, two samples from the MBE- and two from the OMCVD-grown structures. To prevent excessive overheating, the measurements were performed at a lower applied electric field ( $6.5 \text{ kV cm}^{-1}$ )

than the one at laser threshold ( $7.6 \text{ kV cm}^{-1}$ ). As expected from a diagonal transition, at the measurement field, the computed photon energy ( $8.5 \text{ meV}$ ) is lower than the one at which the laser operates ( $11.5 \text{ meV}$ ).

On the same graph is shown the fan chart displaying the energy of the Landau levels as a function of the applied magnetic field, with vertical lines showing the anticipated maxima where the relevant crossing between the lowest Landau level of the active region crosses the excited Landau levels of the lower states. The two samples grown by MBE (EV1116 and EV1157) show a very good agreement between the predicted and observed locations of the maxima; while the two OMCVD samples (3057A and 3057B) show more discrepancies between the experimental and theoretical quantities. These results prove that this design is robust and can accommodate some layer thickness variations. In fact, our attempts to grow ‘conventional’ phonon extraction designs using OMCVD or InGaAs/AlInAs/InP material systems failed while these ‘bound-to-continuum’ designs operated nicely. In addition, the better agreement with the theory shown by sample 3057B as compared with 3057A correlates well with the better optical performances as well as with the better interface quality shown by the sample misoriented towards (111)B. A further understanding of the temperature dependence of our device can be achieved by comparing the magnetotransport at low and high temperatures. Such comparison was carried out for sample EV1116 and is displayed in figure 10(b). As the data were measured in continuous wave, the actual lattice temperature is 20–30 K higher than the one of the holder (130 K) due to self-heating of the device. At this temperature, all transport features have disappeared until about 7 T. This magnetic field corresponds to a cyclotron energy of  $12.3 \text{ meV}$  approximately equal to the photon energy. As the magnetotransport does not depend on the respective population of the lower and upper states, the absence of structure in the magnetotransport for an inter-Landau level spacing equal to the photon energy means that the selectivity of the injection process is lost. In the limit of large in-plane scattering ( $\Omega\tau_{\parallel} \ll 1$ ), the injection efficiency between the upper and lower states of the laser transition should be

$$\eta = \frac{\Omega_i^2}{\Omega_i^2 + \Omega_l^2} \approx 0.8 \quad (4)$$

where  $\Omega_l$  is the coupling strength of the injector into the lower state of the laser transition. The absence of features in magnetotransport therefore means that parasitic injection into other states should be also considered. Low injection efficiency and a poor ratio of lifetimes are responsible for the maximum operating temperature observed in this structure.

## 6. Distributed feedback QCL

Applications of terahertz quantum cascade lasers for spectroscopy and imaging require a well-controlled single-frequency emission, high optical power combined with a good beam quality. We have recently demonstrated that these characteristics can be all achieved by patterning a metal–metal waveguide device with a distributed feedback grating tuned to match the third-order Bragg diffraction condition. Using a deeply etched period structure it is possible to enable an efficient outcoupling of the emitted radiation. However, in contrast to the emission in the vertical direction obtained in second-order-grating DFB lasers, in the third-order case the radiation is emitted along the ridge of the device. Devices operated in the fundamental transverse mode have a symmetric far-field characterized by a low divergence angle of about  $8^\circ$  [43]. The devices shown in figure 11 operate in a higher lateral mode and have therefore a broader

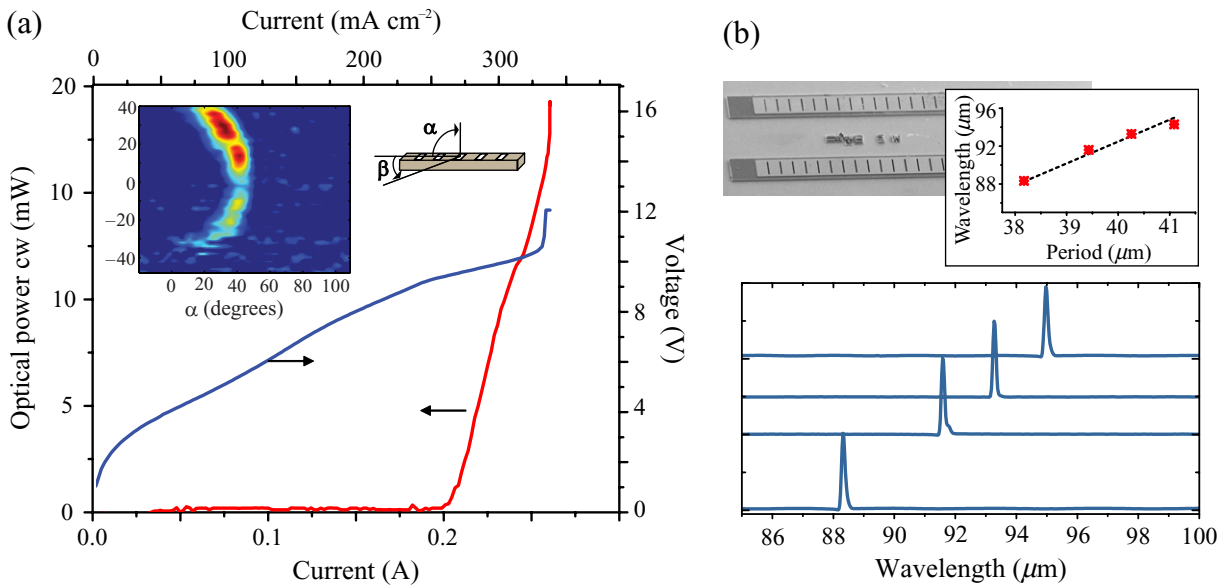


**Figure 11.** (a) Light and voltage versus current for a distributed feedback quantum cascade laser operating single mode, measured at a temperature of 10 K. The operation is on a higher order transverse mode, as shown by the far-field characteristics shown in the inset. The slope efficiency is  $400 \text{ mW A}^{-1}$ . (b) Emission spectrum from distributed feedback devices with various grating periodicities. Insets: scanning electron micrograph of a real device. Tuning of the laser emission with the grating period compared with the third-order Bragg condition (dashed line).

far-field in the lateral direction, as shown in the inset of figure 11(a). As shown in this figure, due to the larger outcoupling losses enabled by the distributed feedback grating the devices achieve a large slope efficiency of  $400 \text{ mW A}^{-1}$  in continuous-wave operation, while the emission remains single mode, as shown in figure 11(b).

## 7. Conclusion

In this paper, the performance characteristics of a device consisting of a bound-to-continuum diagonal active region coupled by resonant tunneling to a single-quantum-well extractor were studied. At low temperature, this device operates with a very low threshold and a high internal differential efficiency. Compared with resonant phonon designs with a single lower state, this design offers a somewhat relaxed constraint on the alignment of the extraction stage, and therefore was found more forgiving in growth thickness fluctuations. As found in other resonant phonon designs, the high temperature operation is limited by the ratio of upper to lower state lifetime and the injection selectivity. It is clear that the mechanism that limits the high temperature operation of the terahertz quantum cascade laser is very different for the mid-infrared and the terahertz. In the mid-infrared device, the temperature dependence of the threshold current density is dominated by the upper state lifetime, because the dephasing mechanisms, driven by interface roughness scattering, are roughly temperature independent. In contrast, in the terahertz, the difficulty in finding a structure with a robust population inversion is

compounded by the problem of insuring a high injection efficiency, as the dephasing mechanism is strongly temperature dependent, being driven by optical phonon scattering.

## Acknowledgments

The helpful collaboration of Kemal Celebi for the magnetotransport measurements is gratefully acknowledged. This work was supported in part by the Swiss National Science Foundation and the NCCR ‘quantum photonics’.

## References

- [1] Siegel P 2002 *IEEE Trans. Microw. Theory Tech.* **50** 910
- [2] Tonouchi M 2007 *Nat. Photon.* **1** 97
- [3] Bolivar P, Nagel M, Richter F, Brucherseifer M, Kurz H, Bosserhoff A and Buttner R 2004 *Phil. R. Trans. Soc. A* **362** 323
- [4] Becklin E E, Tielens A G G M, Gehrz R D and Callis H H S 2007 *Infrared Spaceborne Remote Sens. Instrum. XV* **6678** 8
- [5] Belkin M A, Capasso F, Xie F, Belyanin A, Fischer M, Wittmann A and Faist J 2008 *Appl. Phys. Lett.* **92** 201101
- [6] Faist J, Capasso F, Sivco D, Sirtori C, Hutchinson A and Cho A 1994 *Science* **264** 553
- [7] Köhler R, Tredicucci A, Beltram F, Beere H, Linfield E, Davies A, Ritchie D, Iotti R and Rossi F 2002 *Nature* **417** 156
- [8] Ajili L, Scalari G, Hofstetter D, Beck M, Faist J, Beere H, Davies G, Linfield E and Ritchie D 2002 *IEE Elect. Lett.* **38** 1675
- [9] Scalari G, Ajili L, Faist J, Beere H, Linfield E, Ritchie D and Davies G 2003 *Appl. Phys. Lett.* **82** 3165
- [10] Williams B, Callebaut H, Kumar S, Hu Q and Reno J 2003 *Appl. Phys. Lett.* **82** 1015
- [11] Williams B, Kumar S, Callebaut H, Hu Q and Reno J 2003 *Appl. Phys. Lett.* **83** 2124
- [12] Kumar S, Hu Q and Reno J L 2009 *Appl. Phys. Lett.* **94** 131105
- [13] Ajili L, Scalari G, Faist J, Beere H, Linfield E, Ritchie D and Davies G 2004 *Appl. Phys. Lett.* **85** 3986
- [14] Worrall C, Alton J, Houghton M, Barbieri S, Beere H, Ritchie D and Sirtori C 2006 *Opt. Express* **14** 171
- [15] Walther C, Scalari G, Faist J, Beere H and Ritchie D 2006 *Appl. Phys. Lett.* **89** 231121
- [16] Walther C, Fischer M, Scalari G, Terazzi R, Hoyler N and Faist J 2007 *Appl. Phys. Lett.* **91** 131122
- [17] Darmo J, Tamosiunas V, Fasching G, Kröll J, Unterrainer K, Beck M, Giovannini M, Faist J, Kremser C and Debbage P 2004 *Opt. Express* **12** 1879
- [18] Lee A, Qin Q, Kumar S, Williams B, Hu Q and Reno J 2006 *Appl. Phys. Lett.* **89** 141125
- [19] Kim S *et al* 2006 *Appl. Phys. Lett.* **88** 153903
- [20] Gao J *et al* 2005 *Appl. Phys. Lett.* **86** 244104
- [21] Rabanus D, Graf U U, Philipp M, Ricken O, Stutzki J, Vowinkel B, Wiedner M C, Walther C, Fischer M and Faist J 2009 *Opt. Express* **17** 1159
- [22] Faist J, Capasso F, Sirtori C, Sivco D, Hutchinson A and Cho A 1995 *Appl. Phys. Lett.* **66** 538
- [23] Faist J, Beck M, Aellen T and Gini E 2001 *Appl. Phys. Lett.* **78** 147
- [24] Tredicucci A, Capasso F, Gmachl C, Sivco D, Hutchinson A and Cho A 1998 *Appl. Phys. Lett.* **73** 2101
- [25] Rochat M, Hofstetter D, Beck M and Faist J 2001 *Appl. Phys. Lett.* **79** 4271
- [26] Barbieri S, Alton J, Beere H, Fowler J, Linfield E and Ritchie D 2004 *Appl. Phys. Lett.* **85** 1674
- [27] Williams B, Kumar S, Qin Q, Hu Q and Reno J 2006 *Appl. Phys. Lett.* **88** 261101
- [28] Luo H, Laframboise S R, Wasilewski Z R, Aers G C, Liu H C and Cao J C 2007 *Appl. Phys. Lett.* **90** 041112
- [29] Scalari G, Terazzi R, Giovannini M, Hoyler N and Faist J 2007 *Appl. Phys. Lett.* **91** 032103
- [30] Scalari G, Hoyler N, Giovannini M and Faist J 2005 *Appl. Phys. Lett.* **86** 181101

- [31] Kumar S, Williams B, Hu Q and Reno J 2006 *Appl. Phys. Lett.* **88** 121123
- [32] Faist J 2007 *Appl. Phys. Lett.* **90** 253512
- [33] Lloyd-Hughes J, Delley Y, Scalari G, Fischer M, Liverini V, Beck M and Faist J 2009 unpublished
- [34] Terazzi R, Gresch T, Wittmann A and Faist J 2008 *Phys. Rev. B* **78** 4
- [35] Unuma T, Yoshita M, Noda T, Sakaki H and Akiyama H 2003 *J. Appl. Phys.* **93** 1586
- [36] Rochat M, Ajili L, Willenberg H, Faist J, Beere H, Davies G, Linfield E and Ritchie D 2002 *Appl. Phys. Lett.* **81** 1381
- [37] Sirigu L, Rudra A, Kapon E, Amanti M I, Scalari G and Faist J 2008 *Appl. Phys. Lett.* **92** 181111
- [38] Ajili L, Scalari G, Giovannini M, Hoyler N and Faist J 2006 *J. Appl. Phys.* **100** 043102
- [39] Liu H, Wächter M, Ban D, Wasilewski Z, Buchanan M, Aers G, Cao J, Feng S, Williams B and Hu Q 2005 *Appl. Phys. Lett.* **87** 141102
- [40] Benz A, Fasching G, Andrews A, Martl M, Unterrainer K, Roch T, Schrenk W, Golka S and Strasser G 2007 *Appl. Phys. Lett.* **90** 101107
- [41] Scalari G, Walther C, Sirigu L, Sadowski M, Beere H, Ritchie D, Hoyler N, Giovannini M and Faist J 2007 *Phys. Rev. B* **76** 115305
- [42] Scalari G, Walther C, Fischer M, Terazzi R, Beere H, Ritchie D and Faist J 2009 *Laser Photonics Rev.* **3** 45
- [43] Amanti M I, Fischer M, Scalari G, Beck M and Faist J 2009 *Nature Photonics* **3** 586